

Soft and large-area robot skin for tactile sensing

Author: Karolis Juzikis

Student number: 1810634

RBT number: RBTBEP25008

Supervisor: Hyosang Lee

Bachelor program: Bachelor Of Science in Mechanical Engineering

Robotics section of the Mechanical Engineering department

Date: 2025-07-13

Abstract—Soft tactile sensing plays a critical role in enabling robots to have safe and responsive interactions with humans and their environment. This project presents a scalable system that uses barometric pressure sensors embedded in silicone, combined with a multilayer perceptron (MLP) trained on synthetic data to achieve super-resolution. The training data is generated via finite element (FE) simulations of stress fields under varied indentation conditions. The MLP estimates the full stress distribution from five sensor readings. Preliminary experimental validation shows promising results, with accurate force localization ($MAE = 1.66 \text{ mm}$, $R^2 = 0.978$) and moderate force magnitude estimation ($MAE = 1.01 \text{ N}$, $R^2 = 0.732$). While the system shows potential, further work is needed to improve boundary accuracy, address sensor variability, and evaluate performance across more diverse contact conditions.

I. INTRODUCTION

Soft tactile sensing plays a critical role in enabling robots to have safe and responsive interactions with their environment. By mimicking the compliance and distributed sensing of human skin, soft sensor systems enhance safety during contact and allow robots to detect and respond to physical interactions more effectively.

One enhancement to these systems is the use of super-resolution techniques. Super-resolution refers to computational methods that reconstruct fine-scale contact information from coarse or sparse sensor measurements. This allows for high spatial accuracy without the need for densely packed sensor arrays.

When combined with super-resolution, soft tactile sensing reduces system cost and complexity by minimizing the number of physical sensors required, offering a scalable solution for large or geometrically complex surfaces. The sensors are embedded within an elastic layer, which not only enables pressure distribution for super-resolution but also provides physical protection. If damaged, only the silicone layer needs to be repaired or replaced, which makes the system more robust and maintainable compared to traditional systems, where the sensing elements are exposed.

One promising approach to soft tactile sensing is the use of barometric pressure sensors. These sensors are originally designed to measure air pressure but can be repurposed into high-performance tactile arrays using standard PCB fabrication and silicone molding techniques [1]. These sensors offer several key advantages: they are extremely affordable (as little as \$1 per unit), digitally addressable, and sensitive enough to detect sub-Newton contact forces with excellent linearity. Mechanical stress distribution through the elastic layer naturally enables super-resolution, as pressure spreads across multiple sensors. This allows for spatial decoding through models based on solid mechanics or methods based on machine learning.

Mechanically, these systems are based on the principles of solid elasticity, where applied contact forces propagate through the elastic layer and generate measurable stress or strain at the sensor locations. Tactile force reconstruction has been a long-standing research topic, with early foundational work dating back to 1985 by Fearing and Hollerbach [2], who derived analytical relationships between surface forces

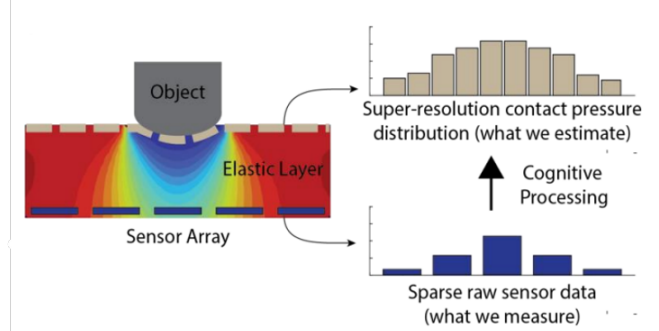


Fig. 1: Concept of super-resolution tactile sensing. Sparse sensor measurements collected from a barometric sensor array embedded in a soft elastic layer are processed to reconstruct a high-resolution contact pressure distribution. Taken from the project description by H. Lee, 2025.

and subsurface strain using sparse sensor data. This work demonstrated early interest in the use of solid mechanics to infer contact information from internal measurements.

A widely adopted method for super-resolution tactile sensing is end-to-end learning using multilayer perceptrons (MLPs) trained on experimental data [3], [4]. Although these models can achieve high accuracy, they come with major limitations. They are highly sensitive to minor changes in the setup, including variations in material, sensor misalignment, or mechanical wear, requiring complete retraining and new data collection. Moreover, the training data is constrained by what can be physically realized, typically limited to single-contact predetermined indenter geometries and only surface-normal contact forces. As a result, collecting sufficient real-world data to cover diverse conditions is both time-consuming and difficult to generalize, making this approach impractical for large-scale or complex systems with varying input parameters.

To overcome these limitations, this project proposes an alternative approach that relies on synthetic data generated by the finite element method (FEM) rather than real-world experimental measurements. The model is designed to map pressure sensor readings from a 1D barometric sensor array to a reconstructed 2D stress field. The primary goal of this project is to develop a contact pressure prediction model that enables this mapping, using only simulated data for training. Although this method may involve a slight reduction in prediction accuracy compared to end-to-end models trained on physical data, it provides several important advantages. It enables faster and more scalable data generation, supports a broader range of contact conditions, and offers greater adaptability to varying geometries and material properties.

These characteristics make the proposed approach more scalable and better suited for real-world applications where flexibility, robustness, and ease of manufacturing are essential. This report presents the design, simulation, training, and experimental validation of the proposed super-resolution sensing system.

II. RELATED WORK

A. Solid mechanics for tactile sensing

Early work in tactile sensing, such as that by Fearing and Hollerbach [2], applied linear elasticity theory to infer contact forces from strain measurements in a soft medium. Their analytical model assumed an infinite elastic half-plane and idealized contact geometries, providing closed-form solutions for estimating force magnitude and location. However, the assumptions of perfect incompressibility, infinite domain, and point contacts restrict the practical applicability of the model.

Experimental studies, including those by Vásárhelyi et al. [5], showed that the strain fields in finite-sized tactile layers deviate significantly from the idealized infinite-plane predictions. Notably, edge effects and thickness variations alter the stress distribution, indicating that more accurate modeling is needed for real-world applications.

Recent approaches, such as those of Wasko et al. [6], apply the Boussinesq–Cerruti and Love solutions to solve inverse elasticity problems and estimate the distributed contact pressure from sparse data. These allow for super-resolution reconstructions but still rely on infinite-domain assumptions and are only accurate away from boundaries and for simple geometries. As such, physically grounded models offer improved resolution but still face limitations in capturing boundary-aware stress fields in practical setups.

B. FEM usage in tactile sensing

There is a growing trend toward the use of simulation-based tools in the development of soft tactile sensors. For example, Zhao et al. [7] leverage FEM simulations to estimate the stiffness matrix \mathbf{K} , which enables inverse FEM to reconstruct dense 3D contact force fields from vision-based tactile input. Similarly, Piacenza et al. [4] utilize quasi-static FEM to optimize sensor placement and geometry in soft, curved tactile arrays. This improves localization accuracy by enhancing mechanical cross-talk between sparse taxels. Building on this direction, Sun and Martius [8] combine FEM simulations with an analytical framework based on taxel value isolines to guide tactile sensor design. Their method quantifies spatial resolution, sensitivity, and contact pattern distinguishability prior to physical fabrication, enabling informed design decisions early in the development process.

C. Simulation-to-real learning and synthetic data generation

Although FEM has been used in tactile sensing to inform sensor design and validate analytical models, its use as a direct data source for machine learning remains rare due to concerns about generalization and realism. Narang et al. [9] address this gap by demonstrating that FEM-simulated deformation fields can be effectively used to train models that generalize to real-world tactile interactions.

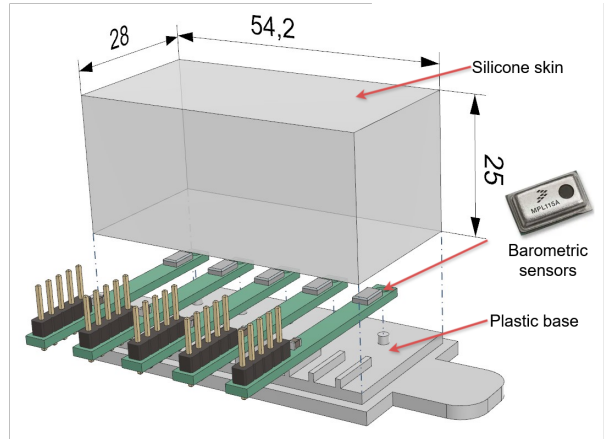
The model learns latent representations for both FEM deformations and real BioTac electrode signals via variational autoencoders and aligns them through a supervised projection. This enables accurate prediction of electrical signals and contact patches for previously unseen objects and interactions,

using only a small amount of labeled real data. Unlike previous methods that rely solely on experimental datasets with limited scope, their approach leverages synthetic data to achieve broader generalization with reduced real-world data collection.

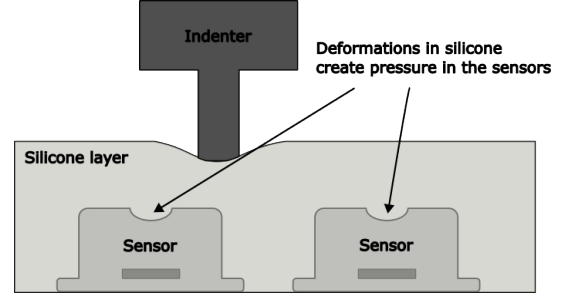
This establishes that simulation-generated tactile data, when coupled with latent-space alignment, provides a viable and efficient alternative to exhaustive physical sampling, supporting scalable learning across diverse contact scenarios [9].

III. SENSOR SETUP

This section delves into the details of the real-life sensor setup after which the FEM simulation was modeled. The setup consists of barometric sensors encased in an elastic silicone layer, shown in Figure 2. This chapter will explain the circuitry of the sensor setup, silicone molding, as well as the sensitivity and accuracy of the sensors.



(a) Exploded view of barometric sensor skin setup



(b) Cross-sectional view of the barometric sensor skin. Deformation from an external indenter propagates through the silicone layer, generating internal pressure detected by the embedded sensors.

Fig. 2: Barometric sensor skin setup

A. Electronics

The setup consists of five MPL115A2 barometric sensors, which are developed to measure air pressure. Each sensor includes a MEMS pressure transducer, ADC, temperature sensor, and I2C communication circuitry, enabling direct integration into PCBs without requiring external signal conditioning. The datasheet lists the range for these sensors as 50 - 115 kPa

with a resolution of 0.15 kPa; however, validated through experiments and other articles using these same sensors [1], the actual range of these sensors is 50-150 kPa, which is essential for this application.

All sensors share the same I2C address and communicate over common SDA and SCL lines. To resolve address conflicts, an MCP23017 I/O expander is used to control the RST pins of the sensors, allowing only one sensor to be active at a time. The expander provides 16 GPIO lines, allowing for the control of up to 16 sensors. A custom Arduino firmware sequentially enables each sensor via the expander, reads pressure data from the shared I2C bus, and sends the data over serial to a host computer. This process occurs in quick succession and completes a read of all sensor values within approximately 50 ms. Two $4.7\text{ k}\Omega$ pull-up resistors are used on the shared SDA and SCL lines.

Each MPL115A2 sensor is powered through shared VCC and GND lines, and a single $1\mu\text{F}$ capacitor is placed between VCC and GND near one of the sensors, as suggested by the datasheet. This capacitor helps suppress voltage fluctuations and transient noise across the power rail, ensuring stable operation for all sensors. In addition, the MPL115A2 datasheet also specifies placing a $1\mu\text{F}$ capacitor between the CAP and GND pins of the sensor. This capacitor supports the sensor's internal reference circuitry and is required for proper operation.

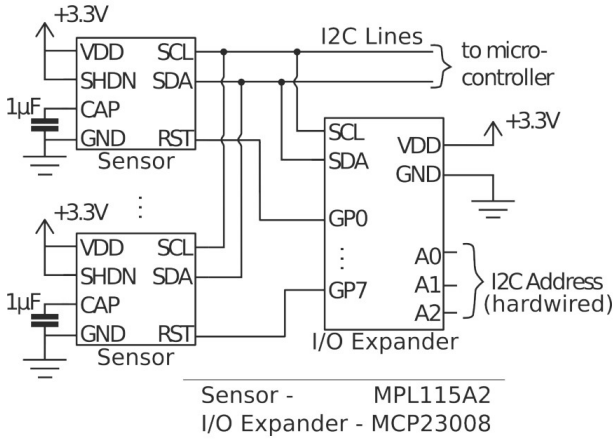


Fig. 3: Circuit example for connecting multiple MPL115A2 barometric sensors to a single I2C bus using an MCP23008 I/O expander. Taken from Tenzer et al. [1].

B. Silicone molding

The dimensions of the setup play a vital role in the resulting precision of the system. According to isoline theory [8], the sensor spacing should be less than twice the thickness of the elastic layer, with even smaller ratios recommended for finer resolution. In this design, the sensor spacing is 10 mm, while the elastic layer is 25 mm thick—intentionally selected to target high-resolution performance. At the same time, the relatively wide spacing allows coverage of a larger area using only five sensors, making the system more tolerant to human

and calibration error, and the uncertainty in precision of the test setup described in subsection V-A. The first and last sensors are positioned 7.1 mm from the boundaries.

The mold for the silicone consists of four parts: top, base, and two side walls. The mold was 3D printed and secured with bolts to ensure a water-tight seal. The mold has an injection and ejection holes, which are used to fill the mold with silicone while allowing the air trapped inside to escape. The silicone molding follows a standard procedure of applying non-stick spray to the mold, filling it with silicone once again to compensate for the volume lost, and curing in the oven. Proper vacuum degassing is a crucial step since it removes air trapped inside the sensor vent hole, which greatly increases the sensor sensitivity [1].

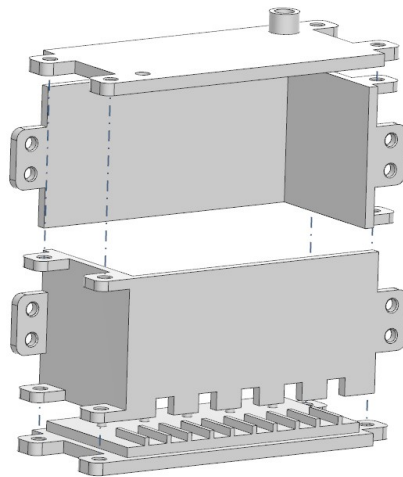


Fig. 4: Exploded view of the 3D-printed silicone mold

Dragon Skin 20 was chosen for its material properties. Stiffer silicones provide greater pressure variation [3], and it was the stiffest material available at the time.

C. Sensor sensitivity and noise

Due to imperfections in the silicone molding process, the sensors exhibit different baseline pressure readings ranging from 64 kPa to 105 kPa. However, this variation had minimal impact on the final predictions, as the pressure difference Δp_{sensor} was used instead of the absolute values. This variation primarily highlights inconsistencies in the molding process. The more detrimental factor is the difference in sensor sensitivities, which is visualized in Figure 5.

In addition to varying sensitivity, the sensor array also suffers from parameter redundancy and spatial ambiguity. As shown in Figure 6, adjacent indentation positions sometimes produce overlapping or nearly identical sensor responses. This leads to a loss of uniqueness in the input-output mapping, making it difficult for the model to precisely determine the contact location. The heatmap also reveals noisy gradients,

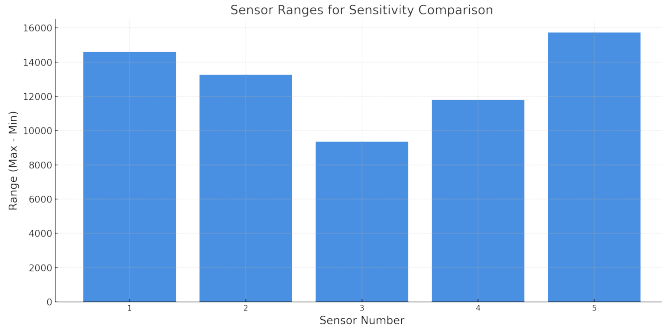


Fig. 5: Different sensor sensitivities across the array

where the expected smooth transition in sensor activation is disrupted by irregularities.

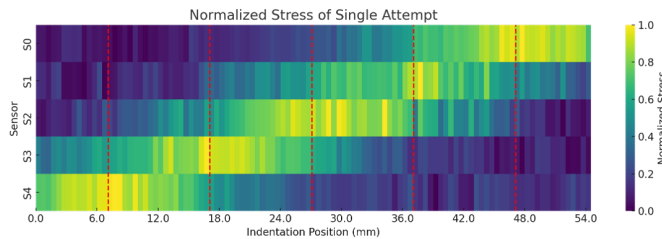


Fig. 6: Normalized stress readings across all sensors for a range of indentation positions. Red dashed lines indicate sensor positions.

IV. SUPER RESOLUTION

This section outlines the development process of the super-resolution approach. It details each step involved, visualized in Figure 7, starting with recreating the real-world sensor setup using FEM. Training data is then generated by simulating various input conditions, such as changes in force location and magnitude. An MLP model is trained to predict the resulting stress fields, which are subsequently post-processed to extract the contact pressure.

A. Finite element modeling

During this project, the FEM calculations were performed in Python utilizing the FEniCS Project [10], composed of multiple Python-based packages with functions to create computational meshes and solve partial differential equations (PDE). This software was chosen for its integration with Python to use it seamlessly in combination with other packages, which are needed for efficient data collection, the development of super resolution, and full control over all computational processes.

FEM modeling was done by establishing a governing PDE derived from the balance of linear momentum and the linear elastic constitutive relations, which is then solved for all elements in the mesh [11], [12]. We seek the displacement field \mathbf{u} such that

$$\int_{\Omega} \boldsymbol{\sigma}(\mathbf{u}) : \boldsymbol{\epsilon}(\mathbf{v}) \, dx = \int_{\Omega} \mathbf{f} \cdot \mathbf{v} \, dx + \int_{\partial\Omega_N} \mathbf{T} \cdot \mathbf{v} \, ds, \quad (1)$$

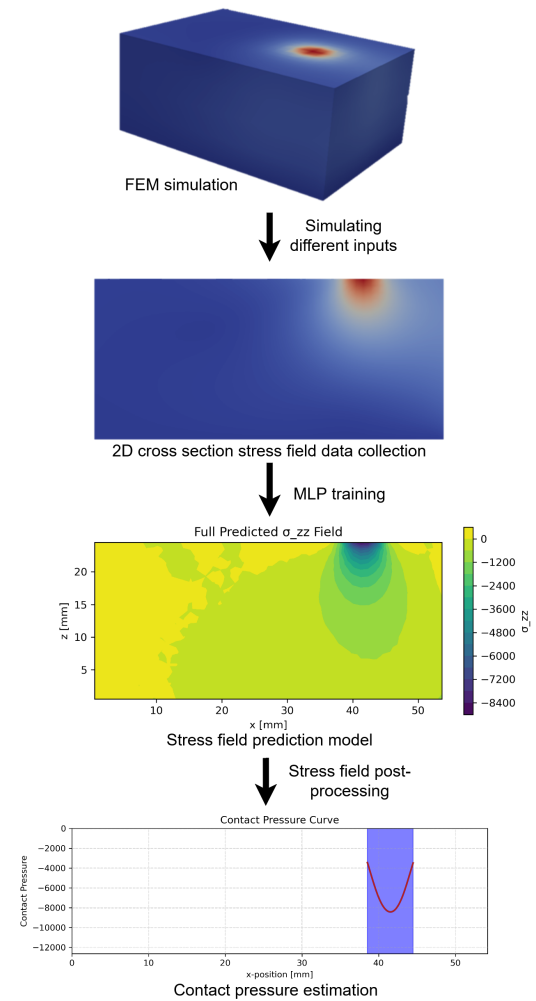


Fig. 7: Workflow for super-resolution contact pressure estimation.

for all test functions $\mathbf{v} \in \hat{V}$.

The stress tensor $\boldsymbol{\sigma}(\mathbf{u})$ is given by

$$\boldsymbol{\sigma}(\mathbf{u}) = \lambda(\nabla \cdot \mathbf{u})\mathbf{I} + \mu(\nabla \mathbf{u} + (\nabla \mathbf{u})^T), \quad (2)$$

and the strain tensor $\boldsymbol{\epsilon}(\mathbf{v})$ is defined as

$$\boldsymbol{\epsilon}(\mathbf{v}) = \frac{1}{2}(\nabla \mathbf{v} + (\nabla \mathbf{v})^T). \quad (3)$$

Where:

- \mathbf{u} : Displacement field.
- \mathbf{v} : Test function (virtual displacement).
- $\boldsymbol{\sigma}$: Cauchy stress tensor.
- $\boldsymbol{\epsilon}$: Linearized strain tensor.
- λ, μ : Lamé parameters.
- \mathbf{I} : Identity tensor.
- \mathbf{f} : Body force per unit volume.
- \mathbf{T} : Traction on the Neumann boundary $\partial\Omega_N$.
- Ω : The domain of the solid body.

- $\partial\Omega_N$: Portion of the boundary, where Neumann (traction) conditions are applied.

Although silicone rubber follows a non-linear stress-strain curve, it was approximated as linear in this work because under small deformations its stress-strain response is nearly linear. This simplification allows for a more efficient solution and reduces the number of material parameters, which can vary significantly between cases. A linear elastic model can accurately approximate the mechanical behavior of silicone when the deformations are small, typically below 20–30%, as is common in tactile sensing applications [7].

In the simulation, two distinct boundary conditions were applied. A Dirichlet boundary condition was applied to the bottom surface of the silicone ($z = 0$), constraining displacement in all directions to represent a fixed base. The Neumann boundary condition was applied to simulate the input pressure as surface traction. The traction was localized using a masking function, which defined a circular region with radius $r = 3\text{mm}$ centered at a specified position on the surface.

$$t = \begin{cases} -T \cdot n & \text{if } \|x - x_0\| < r \\ 0 & \text{otherwise} \end{cases} \quad (4)$$

Here, n is the outward unit normal, x_0 is the center of the loaded region, and T is the prescribed traction magnitude. This was meant to replicate the indenter contact of the same radius in real life.

The Young's modulus was defined based on a study that characterized the linear elastic behavior of Dragon Skin 20 under small deformations [13]. The material was modeled as nearly incompressible, a common assumption for soft silicones, with a Poisson's ratio of $\nu = 0.48$ and a Young's modulus of $E = 0.47\text{MPa}$.

The FEM model employs a 3D hexahedral mesh consisting of $48 \times 9 \times 24$ elements along the X , Y , and Z directions, respectively. This meshing strategy prioritizes high resolution in the XZ plane, where the stress field is extracted, while keeping the computational cost manageable by reducing the number of elements along the Y -axis. The model uses first-order Lagrange (linear) elements, which provide a balance between computational efficiency and spatial accuracy for capturing stress distributions under contact loading.

B. Data collection

To develop an accurate contact pressure prediction model, it is essential to gather a diverse dataset comprising distinct inputs for effective model training. In this work, the data were generated using FEM simulations.

Due to the scope and limitations of the project, the goal is to analyze the 2D stress field at a cross-section. However, a full 3D simulation is necessary to capture the true mechanical response, as a 2D model cannot account for out-of-plane stress distribution, the full contact area of the circular indenter, or the influence of 3D boundary conditions. The 3D model ensures these effects are accurately represented, even though the stress analysis focuses on a 2D slice.

The barometric sensors are designed to measure atmospheric pressure. In this case, it is assumed that the sensor reading represents the stress in the Z direction at the sensor location, i.e., $\Delta P_{\text{measured}} = \sigma_{zz}$. This assumption is justified as the sensor has a narrow orifice in the Z direction while being shielded by a metal cap on all other sides. Therefore, the stress field analyzed from this point onward corresponds to the Z -direction stress component.

Two types of data are collected from the simulations:

- **Sensor readings** – an array of 5 σ_{zz} values extracted at the taxel locations corresponding to the real-life sensor setup. These represent the simulated sensor readings.
- **Stress field** – a 48×24 matrix of σ_{zz} values representing the stress distribution across all elements within the domain.

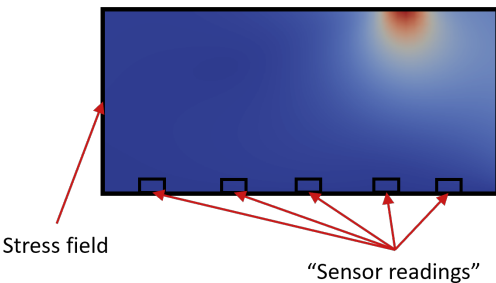


Fig. 8: Cross-sectional view of the simulated stress field (σ_{zz}) generated by a surface contact. The red arrows indicate the locations where pressure values are sampled to simulate readings from the five embedded barometric sensors. These values serve as the input to the machine learning model.

Across simulations, input parameters are varied to generate a diverse and representative dataset. The force is always applied at the top boundary of the skin at $z = 25\text{ mm}$, directly above the sensor located at $y = 14\text{ mm}$. The x -position of the applied force is varied from the left boundary ($x = 0\text{ mm}$) to the right boundary ($x = 54\text{ mm}$) in 1 mm increments, resulting in 55 simulations. For each x -position, the force magnitude is varied from 10^4 N/m^2 to 10^7 N/m^2 in 7 logarithmic steps, giving a total of $55 \times 7 = 385$ simulations.

To increase the resilience of the model, domain randomization is applied by varying uncertain material parameters such as Poisson's ratio and Young's modulus. Following Tiboni et al. [14], introducing variability in these parameters significantly improves system robustness while having minimal impact on accuracy. Therefore, a Gaussian noise is added to the material properties across simulations, with Young's modulus set as $E = 0.47 \times 10^6 \pm 0.02 \times 10^6\text{ Pa}$ and Poisson's ratio as $\nu = 0.48 \pm 0.01$.

C. Multilayer perception training

To estimate the full stress field from limited sensor data, a supervised learning approach is employed using an MLP. The MLP is trained on the dataset generated in the previous

step, where the input \mathbf{X} consists of the simulated sensor readings (an array of σ_{zz} values at selected taxel locations), and the target output \mathbf{Y} is the corresponding full stress field represented as a 48×24 matrix of σ_{zz} values. The goal of the MLP is to learn a mapping function $f : \mathbf{X} \rightarrow \mathbf{Y}$ that accurately reconstructs the full stress distribution from sparse sensor measurements.

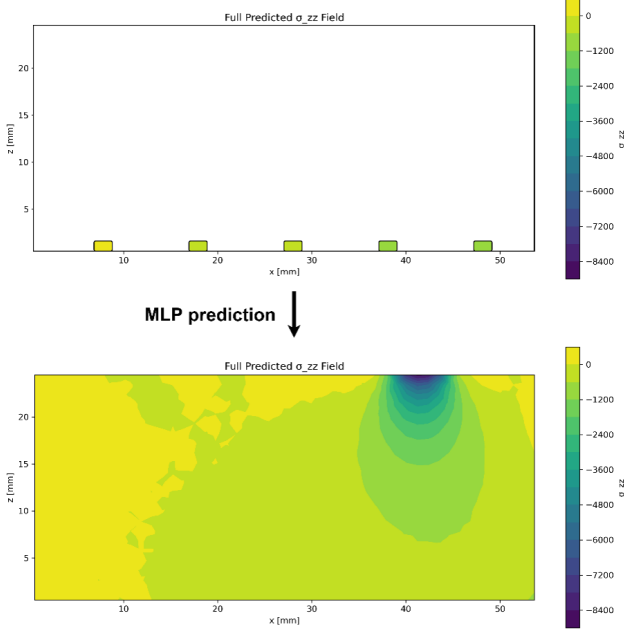


Fig. 9: Top: Measured sensor values from the barometric array, representing the sparse input fed into the MLP. Bottom: Predicted stress field (σ_{zz}) reconstructed by the MLP model. The network infers the full spatial distribution from limited sensor inputs, demonstrating super-resolution reconstruction capability.

To further improve the model's robustness, Gaussian noise with a standard deviation of 2% is added to the simulated sensor readings, reflecting the expected noise level in real-world sensors. Instead of injecting noise directly into the entire dataset, a duplicate of the original dataset is created with added noise, and then appended to the clean data. This approach doubles the training set and ensures that the model learns to generalize from both clean and noisy inputs. Importantly, it encourages the network to learn the true underlying mapping from sensor data to stress fields, rather than fitting to specific noise realizations, thereby increasing robustness without compromising accuracy.

To ensure stable training and balanced feature influence, all data is systematically normalized and scaled. Sensor readings are first normalized per sample to unit norm, emphasizing relative distribution and reducing sensitivity to absolute magnitudes. All input features, including taxel positions and normalized readings, are then standardized using z-score normalization to achieve zero mean and unit variance. The output stress field is scaled using the same per-sample norm to

maintain input-output consistency. These preprocessing steps enhance robustness and enable the model to learn a stable, generalizable mapping from sparse sensor inputs to the full stress field.

The MLP hyperparameters were optimized using cross-validated grid search. The network consists of 4 hidden layers with 256 neurons each. An L2 regularization term of $\alpha = 10^{-5}$ was used. The model was trained using the Adam optimizer with a tanh activation function, a learning rate of 5×10^{-4} , and a maximum of 10,000 iterations. Early stopping was enabled to prevent overfitting.

The model was first evaluated on a test dataset containing data simulated with force locations, magnitudes, and other material parameters that were not present in the training set. It achieved an R^2 score of 0.98, indicating strong predictive performance.

D. Stress field post-processing

This step is necessary to transition from the stress field to measurable quantities in the real-world setup, such as force position, force magnitude, and contact area.

To visualize the stress distribution more clearly, radial basis function interpolation is applied to the stress field. This smoothing step helps produce a continuous representation of the discrete stress data. The point of maximum stress is then identified and taken as the estimated contact center. For comparison and visualization, the highest stress values at the top boundary are also plotted, providing a direct indication of where the force is applied on the surface.

The force is calculated based on the assumption that the surface normal stress is equal to the contact pressure, i.e., $\sigma_{zz} = p_{\text{contact}}$. Therefore, to obtain the force magnitude, the stress along the top boundary is integrated over the estimated contact area obtained in the previous step:

$$F = \int_A \sigma_{zz}(x, y) dA \quad (5)$$

V. REAL DATA COLLECTION

The real-world data was collected to validate and evaluate the super-resolution model trained on simulated FEM data. This chapter provides an overview of the testing setup, describes the function of each component, and outlines the experimental procedures.

A. Testing setup

The testing setup consists of the robot skin described in section III, an XZ stage, a mechanical indenter, and a load cell force sensor.

The indentation is performed using an XZ stage repurposed from an abandoned 3D printer. It enables precise movement in the X and Z directions and serves as the ground truth for the force location.

The load cell force sensor, calibrated to an accuracy of ± 1 gram, provides the ground truth for the applied force magnitude.

The indenter is 3D printed from PLA and features an interchangeable tip with a radius of $r = 3$ mm.

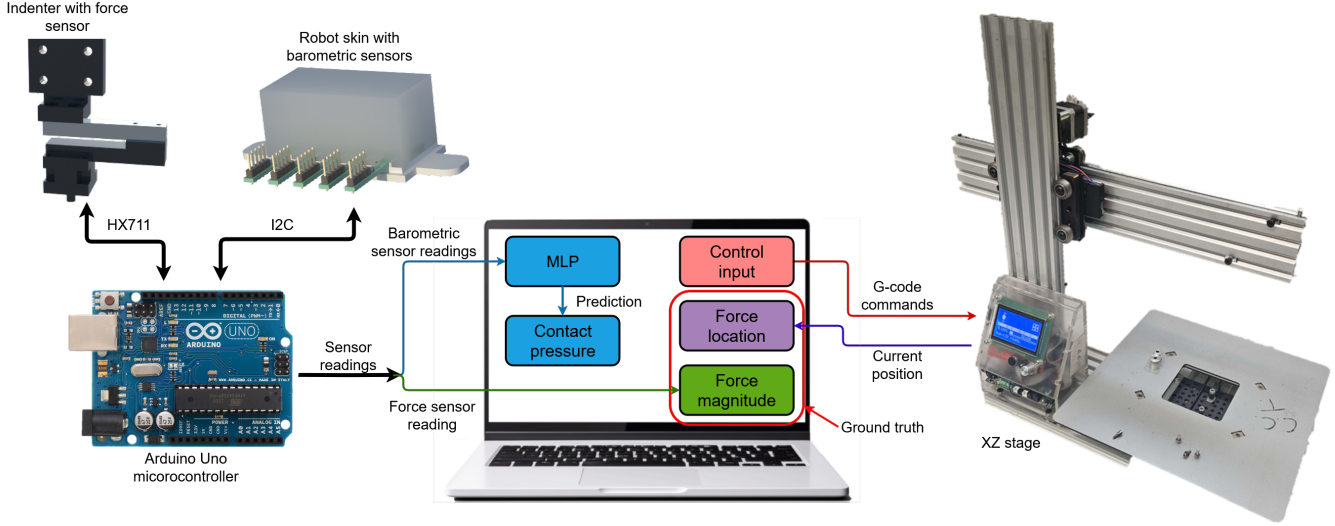


Fig. 10: Overview of the experimental setup with data collection and control architecture

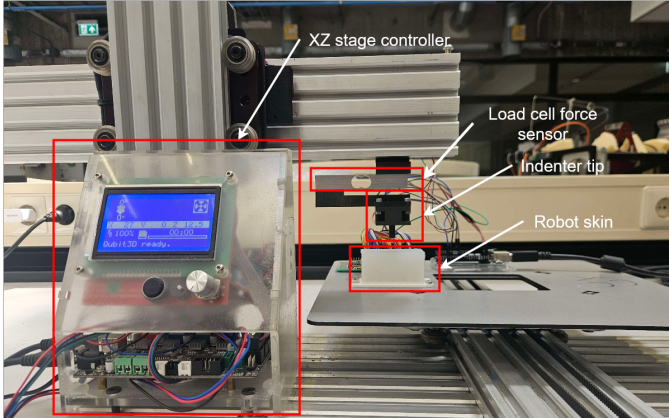


Fig. 11: Component diagram of the testing setup

B. Testing procedure

The testing procedure involves performing multiple indentations along the central line, replicating the same force location pattern used during simulation.

The system is controlled by two Python scripts: one manages data collection and controls the XZ stage for indentation, while the other performs real-time MLP inference to estimate contact pressure, force magnitude, and location. Both scripts operate in real time, and all raw and predicted data are saved to a CSV file for later analysis.

The XZ stage is driven by G-code commands issued via a Python interface. Upon reaching the target coordinate, sensor readings are collected, and the current position is logged as the ground truth for indentation. An Arduino Uno gathers data from both the load cell and barometric sensors and sends it to the host computer, where it is parsed into separate force and pressure streams. The barometric sensor data is passed to the trained MLP, which returns inference results that are

compared to the measured ground truth for validation. The system architecture is illustrated in Figure 10.

VI. RESULTS

This section presents the evaluation of the proposed system, including simulation accuracy, model performance, and experimental validation results. A demonstration video of real-time contact pressure prediction in the physical setup can be found at this link.

A. Force location estimation

The super-resolution model successfully estimated the real contact location with an R^2 score of 0.978 and a mean absolute error (MAE) of 1.66 mm, evaluated over two tests containing 110 data points each. The predicted versus ground truth locations are shown in Figure 12.

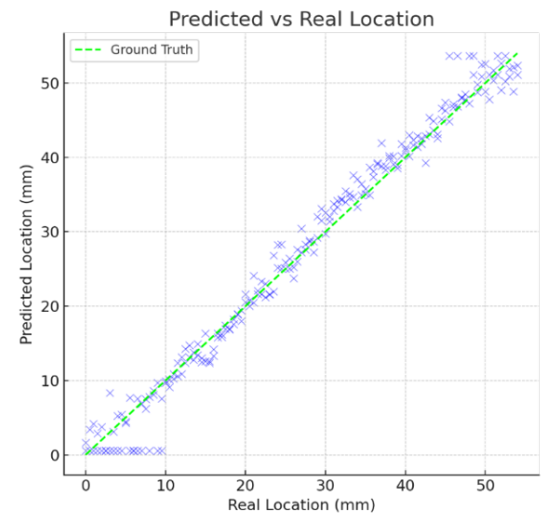


Fig. 12: Predicted versus ground truth force location

The model exhibits reduced accuracy near the boundaries, where predictions deviate more significantly from the actual contact location.

B. Force magnitude estimation

The predicted force magnitude shown in Figure 13 achieved an R^2 score of 0.732 and a MAE of 1.01 N. The model consistently underestimates the true force by approximately 1 N across the dataset, indicating a potential systematic bias.

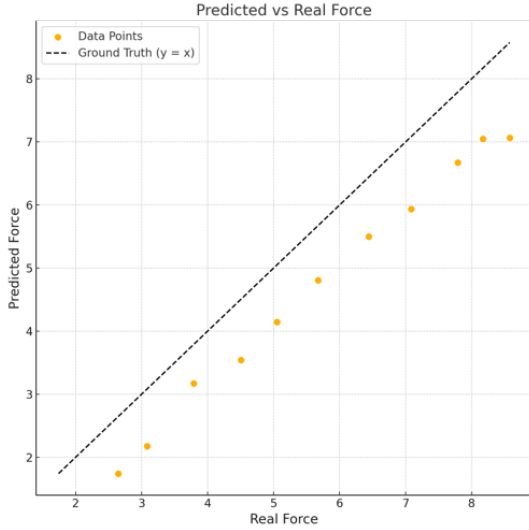


Fig. 13: Predicted versus ground truth force magnitude

VII. DISCUSSION

The results presented in the previous section demonstrate the effectiveness of the proposed super-resolution approach for predicting contact force location and magnitude from sparse sensor inputs. In this section, we analyze the observed performance, highlight limitations, and discuss possible causes of prediction errors and areas for future improvement.

Although the model performed well overall, certain consistent errors were observed—most notably, systematic underestimation of force magnitude by approximately 1 N, and decreased accuracy in localizing contacts near the boundaries of the sensor array. These limitations suggest opportunities for refining both the training data distribution and the model architecture to improve generalization, especially in edge cases.

A. Design Limitations

The current system is constrained by several limitations rooted in the physical sensor setup. One key issue is varying sensor sensitivity, explained in subsection III-C due to small imperfections during silicone molding. These inconsistencies cause the predicted stress field to skew toward more sensitive sensors, increasing the overall prediction error.

The sensor arrangement also suffers from parameter redundancy. Specifically, the ratio of skin thickness to sensor spacing makes it difficult to distinguish between different

contact conditions. For example, a smaller indenter with a higher pressure can produce sensor readings similar to a larger indenter with a lower pressure, making it impossible to infer contact area or pressure distribution uniquely from the current input alone.

Prediction accuracy near the array boundaries is notably poor. Accurate localization typically requires the indentation to influence at least three sensors, which helps reduce uncertainty through averaging of independent noise sources [8]. In the present design, this condition is only met for indentations occurring at ≈ 10 mm away from the boundary.

Force magnitude estimations consistently exhibit an offset of approximately 1 N. This discrepancy may stem from incorrect modeling assumptions, such as treating the measured pressure change as equal to the surface normal stress, i.e., $\Delta p_{\text{measured}} = \sigma_{zz}$, or using the simplified force estimation equation $F = \int_A \sigma_{zz}(x, y) dA$. Additionally, errors in simulation parameters, such as an inaccurate Young's modulus used in the FEM-generated training data, could also contribute to the observed bias.

Extending the system to support non-surface normal indentations or multiple simultaneous contact points was not feasible within the time constraints. Also, doing so would require a completely new test setup and indenter design, and would likely still suffer from the same redundancy issues present in the current setup.

B. Improvements and future work

Future improvements aim to address current limitations in the system design. A key enhancement would be improving the silicone molding process by performing vacuum degassing twice instead of once, and by using brand-new sensors rather than reusing those from failed molding attempts. Reused sensors may retain cured silicone residue that traps air pockets, making it difficult or impossible for newly applied silicone to bond properly or degas completely. This results in trapped air that compromises uniformity. Using new sensors and improved degassing would help eliminate air bubbles more effectively, leading to more consistent sensor sensitivity across the array.

Another improvement involves compensating for variability in sensor sensitivity. Introducing a sim-to-real mapping neural network or involving additional sensor calibration could help mitigate differences in sensor sensitivity while remaining the system more practical than retraining the model using real world data.

To address the parameter redundancy issue, alternative silicone skin thickness-to-sensor spacing ratios should be explored. While the current design aims for high resolution, the 25 mm thick silicone layer is unusually large and may cause spatial blurring or ambiguity in force interpretation, as thicker elastic covers have been shown to attenuate and work as a low pass filter for the pressure [5].

Improving accuracy near the boundaries requires at least three sensors to be activated during indentation. Placing the first sensor closer to the edge and potentially reducing sensor

spacing near the boundaries could enhance resolution in those regions.

The force magnitude estimations can be improved by validating the underlying assumptions using FEM simulations, experimentally estimating the Young's modulus of the silicone material, or applying a linear correction model to compensate for the observed systematic error.

Lastly, future extensions of this work could involve estimating non-normal forces, handling multiple simultaneous contacts with different indenter radii, and extending the method to full 3D stress reconstruction rather than focusing solely on 2D slices.

VIII. CONCLUSION

This project demonstrates that super-resolution tactile sensing using sparse barometric sensors trained exclusively on synthetic FEM data is capable of generalizing input force magnitude and location. The system predicts contact force location and magnitude, with relatively high accuracy (R^2 score of 0.978) for location estimation and acceptable performance for magnitude (R^2 score of 0.732), despite limitations due to sensor variability, spatial ambiguity, and boundary performance. Improvements to sensor setup and super resolution were proposed, including enhanced molding techniques, design modifications, and sim-to-real transfer. The proposed approach enables a scalable, low-cost, and repairable tactile sensing system suitable for robotic applications, with potential for future extension to 3D stress estimation, multi-point, and non-normal contact inference.

ACKNOWLEDGEMENTS

The barometric sensor PCB and the I/O expander circuit were developed by another student, Alberto Sanchez Delgado.

REFERENCES

- [1] Y. Tenzer, L. P. Jentoft, and R. D. Howe, "The feel of mems barometers: Inexpensive and easily customized tactile array sensors," *IEEE Robotics & Automation Magazine*, vol. 21, pp. 89–95, September 2014.
- [2] R. S. Fearing and J. M. Hollerbach, "Basic solid mechanics for tactile sensing," *The International Journal of Robotics Research*, vol. 4, no. 3, pp. 40–54, 1985.
- [3] J. Hou, X. Zhou, and A. Spiers, "Location and orientation super-resolution sensing with a cost-efficient and repairable barometric tactile sensor," *IEEE Transactions on Robotics*, vol. 41, pp. 729–741, 2025.
- [4] P. Piacenza, S. Sherman, and M. Ciocarlie, "Data-driven super-resolution on a tactile dome," *IEEE Robotics and Automation Letters*, vol. 3, no. 3, pp. 1434–1441, 2018.
- [5] G. Vásárhelyi, K. Széll, T. Duchon, T. Tóth, and Z. Szabó, "Effects of the elastic cover on tactile sensor arrays," *Sensors and Actuators A: Physical*, vol. 132, no. 1, pp. 245–251, 2006.
- [6] W. Wasko, A. Albini, P. Maiolino, F. Mastrogiiovanni, and G. Cannata, "Contact modelling and tactile data processing for robot skins," *Sensors*, vol. 19, no. 4, p. 814, 2019.
- [7] C. Zhao, J. Liu, and D. Ma, "ifem2.0: Dense 3-d contact force field reconstruction and assessment for vision-based tactile sensors," *IEEE Transactions on Robotics*, vol. 41, pp. 289–305, 2025.
- [8] H. Sun and G. Martius, "Guiding the design of superresolution tactile skins with taxel value isolines theory," *Science Robotics*, vol. 7, p. eabm0608, 2022.
- [9] Y. Narang, B. Sundaralingam, M. Macklin, A. Mousavian, and D. Fox, "Sim-to-real for robotic tactile sensing via physics-based simulation and learned latent projections," *arXiv preprint arXiv:2103.16747*, 2021.
- [10] "FEniCS Project." <https://fenicsproject.org/>. Accessed: 2025-06-22.
- [11] O. C. Zienkiewicz, R. L. Taylor, and J. Zhu, *The Finite Element Method: Its Basis and Fundamentals*. Butterworth-Heinemann, 7th ed., 2017.
- [12] A. Logg and H. P. Langtangen, "The equations of linear elasticity." <https://jsdokken.com/dolfinx-tutorial/chapter2/linearelasticity.html>, Jul 2025. FEniCSx tutorial, accessed on July 7, 2025.
- [13] D. L. Presti, S. Dall'Orso, S. Muceli, T. Arichi, S. Neumane, A. Lukens, R. Sabbadini, C. Massaroni, M. A. Caponero, D. Formica, E. Burdet, and E. Schena, "An fmri compatible smart device for measuring palmar grasping actions in newborns," *Sensors*, vol. 20, no. 21, p. 6040, 2020.
- [14] G. Tiboni, A. Protopapa, T. Tommasi, and G. Averta, "Domain randomization for robust, affordable and effective closed-loop control of soft robots," *arXiv preprint arXiv:2303.04136*, 2023.